

# Practical Calculation of Nuclear Fusion Power for a Toroidal Plasma Device with Magnetic Confinement

Pavel R. GONCHAROV

*St. Petersburg Polytechnic University, 195251, Russia*

(Received 10 January 2009 / Accepted 19 August 2009)

An algorithm has been developed and realized as a FORTRAN code to calculate the volume integral power of a magnetic confinement nuclear fusion reactor and the local fusion rate function. It takes the nuclei energy distributions, fusion cross-sections, and magnetic surface geometry as input data. Two fast, simple analytic models of magnetic flux surfaces were used, and the corresponding Jacobian determinants were found. Gaussian kernel empirical probability density estimation has been proposed to reconstruct the ion energy probability density function from experimentally obtained random samples of escaping neutral atom energies. The influence of ion heating and fast ion confinement on high-energy distribution tails, and thus on the neutron yield and fusion power, can be calculated. The code has been applied to obtain radial profiles of the nuclear fusion reaction rate and volume integral power for both Maxwellian and suprathermal D and T particle distributions. A fast neutral particle diagnostic database may serve as a basis for an experimentally confirmed calculation technique for reactor power and ignition criterion.

© 2010 The Japan Society of Plasma Science and Nuclear Fusion Research

Keywords: fusion reactor power, nuclear fusion rate, ion distribution function, high-energy particle, non-Maxwellian rate coefficient, empirical probability density

DOI: 10.1585/pfr.5.S1028

## 1. Introduction

The power of a magnetic confinement fusion reactor  $P$  [W] and the fulfillment of the ignition criterion are quantitatively determined by the nuclear fusion reaction rate  $\mathcal{R}_{\alpha\beta}$  [ $\text{m}^{-3}\text{s}^{-1}$ ] integrated over the plasma volume using the known magnetic surface geometry:

$$\begin{aligned} P &\propto \int \mathcal{R}_{\alpha\beta}(\mathbf{r}) d^3\mathbf{r} \\ &= \int \mathcal{R}_{\alpha\beta}(\rho, \vartheta, \phi) R(\rho, \vartheta, \phi) |J| d\rho d\vartheta d\phi. \end{aligned} \quad (1)$$

where

$$J = \begin{vmatrix} \frac{\partial R}{\partial \rho} & \frac{\partial R}{\partial \vartheta} & 0 \\ \frac{\partial Z}{\partial \rho} & \frac{\partial Z}{\partial \vartheta} & 0 \\ 0 & 0 & 1 \end{vmatrix}. \quad (2)$$

is the Jacobian determinant for the transformation from cylindrical coordinates  $(R, Z, \varphi)$  to flux coordinates  $(\rho, \vartheta, \varphi)$ ;  $\rho$ ,  $\vartheta$  and  $\varphi$  are the magnetic surface label, poloidal angle, and toroidal angle, respectively. Azimuthally symmetric magnetic surfaces are assumed in (2).

The rate of the nuclear fusion reaction between species  $\alpha$  and  $\beta$ ,

$$\mathcal{R}_{\alpha\beta} = \frac{n_\alpha n_\beta}{1 + \delta_{\alpha\beta}} \tilde{\mathcal{R}}_{\alpha\beta}. \quad (3)$$

in turn, is proportional to the rate coefficient  $\tilde{\mathcal{R}}_{\alpha\beta} = \langle \sigma(v)v \rangle$  averaged over the velocity distribution functions of the reacting species by integrating over the six-dimensional velocity space

$$\tilde{\mathcal{R}}_{\alpha\beta} = \int \sigma(v) v f_\alpha(\mathbf{v}_\alpha) f_\beta(\mathbf{v}_\beta) d^3\mathbf{v}_\alpha d^3\mathbf{v}_\beta. \quad (4)$$

where  $v = |\mathbf{v}_\alpha - \mathbf{v}_\beta|$  is the relative velocity, and  $\delta_{\alpha\beta}$  is the Kronecker symbol, reflecting the fact that when the reacting species are identical, as in DD and TT reactions, and their density is  $n$ , the rate is proportional to the number of combinations  $C_n^2 = n(n-1)/2 \approx n^2/2$

The FORTRAN code for nuclear fusion rate and power calculation is based on (1)-(4), and nuclear cross-section approximations have been obtained from references [1-3]. Particle density profiles and the magnetic surface geometry are used as input data. The main new feature of the code is that not only analytic fast ion distribution functions based on theoretical models, but also experimentally obtained distributions may be used for the calculations. Suprathermal high-energy particles contribute greatly to the reaction rate. The influence of ion heating and fast ion confinement on high-energy distribution tails, and thus on neutron yield and fusion power, can be calculated on the basis of experimental data.

## 2. Analytic Models of Magnetic Surfaces

A rigorous treatment requires the use of Grad-Shafranov equation solutions. To increase the computation speed and simplify the code, two analytic models of magnetic surfaces have been used, in the form of nested shifted D-shaped curves and nested shifted ellipses in the poloidal cross-section. The D-shaped last closed flux surface (LCFS) equation in cylindrical coordinates is

$$Z_{\text{LCFS}}^{\pm}(R) = \pm \sqrt{(\kappa_1 + \kappa_2 R)} \times \sqrt{\kappa_3 R^2 + \kappa_4 R + \kappa_5 + \kappa_6 R + \kappa_7}. \quad (5)$$

where  $\kappa_1 = R_{\text{out}}/2\gamma$ ,  $\kappa_2 = -1/2\gamma$ ,  $\kappa_3 = 1 - 4\gamma$ ,  $\kappa_4 = -2(\kappa_3 R_{\text{out}} + \delta(2\gamma - 1))$ ,  $\kappa_5 = \kappa_3 R_{\text{out}}^2 + 2\delta \times (2\gamma - 1) R_{\text{out}} + \delta^2$ ,  $\kappa_6 = 1$ , and  $\kappa_7 = \delta - R_{\text{out}}$  are determined by three input parameters: outer plasma radius  $R_{\text{out}}$  [m], LCFS poloidal cross-section width  $\delta$  [m], and dimensionless  $\gamma$  to control the LCFS poloidal cross-section width to height ratio. One more dimensional input parameter  $\Delta$  [m] is used to simulate the Shafranov shift. The magnetic axis position is then

$$R_0 = \frac{R_{\text{in}} + R_{\text{out}}}{2} + \Delta. \quad (6)$$

where the inner plasma radius  $R_{\text{in}}$  [m] is calculated from the LCFS equation (5). The poloidal angle  $\vartheta \in [0, 2\pi)$  is defined in the same way as the polar angle, assuming  $R = R_0, Z = 0$  is the center point and  $R$  is the polar axis.

In the transformation between cylindrical coordinates  $(R, Z, \phi)$  and flux coordinates  $(\rho, \vartheta, \phi)$ , the azimuthal (toroidal) angle  $\phi \in [0, 2\pi)$  is preserved. For a given point  $(\rho, \vartheta)$  in the poloidal plane, the transformation of coordinates to cylindrical  $(R, Z)$  is performed as follows. First,

$$\tilde{\vartheta} = \pi - (\pi - \vartheta) \text{sign}(\pi - \vartheta). \quad (7)$$

is calculated, where  $\text{sign}(y) = -1$  for  $y < 0$  and  $\text{sign}(y) = 1$  for  $y \geq 0$ . If  $\tilde{\vartheta} = 0$ , then  $Z = 0; R = R_0 + \rho(R_{\text{out}} - R_0)$ . If  $\tilde{\vartheta} = \pi$ , then  $Z = 0; R = R_0 + \rho(R_{\text{in}} - R_0)$ . If  $\tilde{\vartheta} = \pi/2$ , then  $R = R_0; Z = \rho Z_{\text{LCFS}}^+(R_0) \text{sign}(\pi - \vartheta)$ . Otherwise, the nonlinear equation

$$\frac{Z_{\text{LCFS}}^+(R_{\text{LCFS}})}{R_{\text{LCFS}} - R_0} - \tan \tilde{\vartheta} = 0. \quad (8)$$

is resolved numerically with respect to  $R_{\text{LCFS}}$ , sought within  $[R_{\text{in}}, R_{\text{out}}]$ . Then,

$$\begin{aligned} R &= R_0 + \rho(R_{\text{LCFS}} - R_0), \\ Z &= \rho Z_{\text{LCFS}}^+(R_{\text{LCFS}}) \text{sign}(\pi - \vartheta). \end{aligned} \quad (9)$$

The ellipse-shaped LCFS equation in cylindrical coordinates is

$$Z_{\text{LCFS}}^{\pm}(R) = \pm \sqrt{\kappa_1 R^2 + \kappa_2 R + \kappa_3}. \quad (10)$$

where  $\kappa_1 = -b^2/a^2$ ,  $\kappa_2 = 2b^2(R_{\text{out}} - a)/a^2$ , and  $\kappa_3 = b^2 - b^2(R_{\text{out}} - a)^2/a^2$  are determined by three dimensional

input parameters: outer plasma radius  $R_{\text{out}}$  [m] and major and minor ellipse semiaxes  $a$  [m] and  $b$  [m]. Again, an additional dimensional input parameter  $\Delta$  [m] is used to simulate the Shafranov shift. The magnetic axis position is then

$$R_0 = R_{\text{out}} - a + \Delta. \quad (11)$$

The coordinate transformation from  $(\rho, \vartheta)$  to  $(R, Z)$  is performed using formulas (8) and (9) as for D-shaped curves, substituting the proper function  $Z_{\text{LCFS}}^+(R)$  given by (10) for (5).

Fig. 1 shows  $\rho = \text{const}$  isolines obtained by using the coordinate transformation procedures for the two model magnetic surface shapes. The parameters are  $\delta = 1.5$  m,  $\gamma = 0.326426$  for Fig. 1 a);  $a = 0.75$  m,  $b = 1.5$  m for Fig. 1 b); and  $R_{\text{in}} = 1.5$  m,  $R_{\text{out}} = 3$  m,  $\Delta = 0.1$  m for both.

Since  $R$  and  $Z$  are implicit functions of  $\rho$  and  $\vartheta$ , central difference derivative formulas are used to calculate the elements of Jacobian determinant (2). Left and right difference derivatives are used at the extremities of the range  $\rho \in [0, 1]$ ,  $\vartheta \in [0, 2\pi)$ . The resulting  $|J|$  shown in Fig. 2 enables calculation of volume integral (1) for either of the two magnetic surface types.

Either these fast simple analytic models, or ones similar to [4, 5], may be used as a satisfactory practical approx-

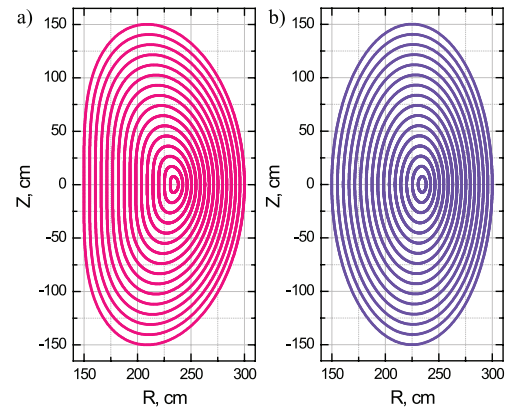


Fig. 1 a) D-shaped and b) ellipse-shaped isolines  $\rho = \text{const}$  for  $R_{\text{in}} = 1.5$  m,  $R_{\text{out}} = 3$  m,  $\Delta = 0.1$  m.

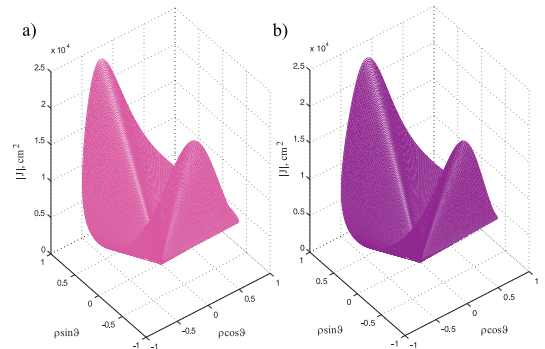


Fig. 2 Jacobian determinant for a) D-shaped and b) ellipse-shaped magnetic surface models.

imation of a tokamak's magnetohydrodynamic (MHD) equilibrium whenever chord or volume integration or mapping of plasma parameters as functions of magnetic surfaces to real space coordinates is required in physical and engineering tasks. For stellarator/heliotron configurations, more complicated full-3D models are needed.

The correctness of Jacobian determinant (2) and the performance of volume integration subroutine (1) can be tested easily by substituting constant unity instead of the reaction rate  $\mathcal{R}_{\alpha\beta}$ . The numerical integration result should then be equal to the volume  $V_{\text{LCFS}}$  enclosed by LCFS, which is readily obtained as

$$V_{\text{LCFS}} = 4\pi \int_{R_{\text{in}}}^{R_{\text{out}}} RZ_{\text{LCFS}}^+(R) dR. \quad (12)$$

in general, and as  $V_{\text{LCFS}} = \pi^2(R_{\text{in}} + R_{\text{out}})ab$  in particular for the ellipse-shaped cross-section case.

### 3. Nuclear Fusion Rate Coefficients

#### 3.1 Monoenergetic beam and Maxwellian target

For the monoenergetic and monodirectional distribution  $f_{\alpha}(\mathbf{v}_{\alpha}) = \delta(\mathbf{v}_{\alpha} - \mathbf{V})$  of species  $\alpha$  interacting with a Maxwellian target  $\beta$ ,

$$f_{\beta}(\mathbf{v}_{\beta}) = f^{(M)} = \left(\frac{m_{\beta}}{2\pi T}\right)^{3/2} e^{-\frac{m_{\beta}v_{\beta}^2}{2T}}. \quad (13)$$

rate coefficient (4) is reduced to

$$\begin{aligned} \tilde{\mathcal{R}}_{\alpha\beta}^{(BM)}(V, m_{\beta}/T) &= \frac{1}{V} \left(\frac{2m_{\beta}}{\pi T}\right)^{1/2} e^{-\frac{m_{\beta}V^2}{2T}} \\ &\times \int_0^{+\infty} v^2 \sigma(v) \sinh\left(\frac{m_{\beta}vV}{T}\right) e^{-\frac{m_{\beta}v^2}{2T}} dv. \end{aligned} \quad (14)$$

Denoting the atomic velocity unit as  $v_0 \approx 2.188 \times 10^8$  cm/s and introducing a dimensionless variable  $y = v^2/v_0^2$  and

dimensionless constants  $A = \frac{m_{\beta}v_0^2}{2T}$  and  $B = V/v_0$ , consider a dimensionless function

$$\mathcal{F}(y) = \sqrt{y} \left( e^{2AB\sqrt{y}-Ay-AB^2} - e^{-2AB\sqrt{y}-Ay-AB^2} \right). \quad (15)$$

Then,

$$\tilde{\mathcal{R}}_{\alpha\beta}^{(BM)}(V, m_{\beta}/T) = \frac{v_0}{2\sqrt{\pi}} \frac{\sqrt{A}}{B} \int_0^{+\infty} \sigma(y) \mathcal{F}(y) dy. \quad (16)$$

To avoid arithmetic overflows, the constant  $e^{-AB^2}$  should not be taken outside the integral.  $\mathcal{F}(y)$  is a nonnegative, slightly asymmetrical bell-shaped exponentially decaying function as shown in Fig. 3. The maximum position depends on the parameters. Qualitatively, function  $\mathcal{F}(y)$  can be thought of very roughly as a Gaussian curve corresponding to the Maxwellian distribution of target particles,

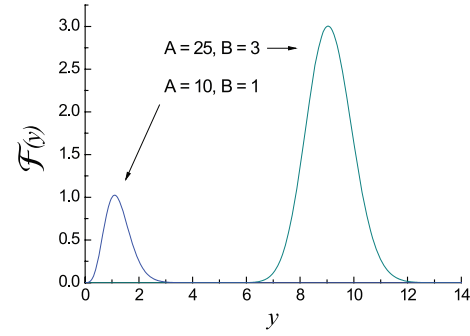


Fig. 3 Function  $\mathcal{F}(y)$  in the integrand of the beam-Maxwellian rate coefficient (16).

shifted along the abscissa axis by a value corresponding to the beam particle velocity. The exact maximum condition is expressed by the nonlinear equation

$$\tanh z = \frac{2AB^2z}{z^2 - 2AB^2}. \quad (17)$$

where  $z = 2AB\sqrt{y}$ . Equation (17) can be solved numerically by taking the positive root of the quadratic equation corresponding to the unit right-hand side as an initial approximation.

Assuming the cross-section  $\sigma(y)$  is a smoother function than  $\mathcal{F}(y)$ , the integral in (16) can first be evaluated over a finite interval around the maximum of  $\mathcal{F}(y)$ . Then, at every subsequent step, one should broaden the initially chosen arbitrary integration limits until the integral value becomes close enough to that obtained at the previous step. Thus, the required relative precision may be achieved.

#### 3.2 Isotropically distributed projectiles and Maxwellian target

If the velocity distribution of species  $\alpha$  is expressed by an isotropic function  $F(v_{\alpha})$ , and the distribution of species  $\beta$  is Maxwellian as in (13), the rate coefficient is calculated as

$$\tilde{\mathcal{R}}_{\alpha\beta}^{(FM)} = 4\pi \int_0^{+\infty} v_{\alpha}^2 F(v_{\alpha}) \tilde{\mathcal{R}}_{\alpha\beta}^{(BM)}(v_{\alpha}, m_{\beta}/T) dv_{\alpha}. \quad (18)$$

The technique to compute  $\tilde{\mathcal{R}}_{\alpha\beta}^{(BM)}(v_{\alpha}, m_{\beta}/T)$  is described above. The practical realization of formula (18) depends on the specific function  $F(v_{\alpha})$ . In particular, for suprathermal ion distributions arising from fast neutral beam injection heating, the upper integration limit, in practice, appears to be finite. Another characteristic case of a bell-shaped exponentially decaying integrand implies that one should step-by-step broaden the integration range around the maximum position, comparing the integral values, until the required relative precision is achieved.

#### 3.3 Isothermal Maxwellian case

This is an important particular case of subsection 3.2. For two Maxwellian species  $\alpha$  and  $\beta$  at thermal equilibrium

$T_\alpha = T_\beta = T$ , the rate coefficient is

$$\tilde{\mathcal{R}}_{\alpha\beta}^{(MM)}(\mu_{\alpha\beta}/T) = \frac{2}{\sqrt{\pi}} v_0 \gamma^{3/2} \int_0^{+\infty} \sigma(y) f(y) dy. \quad (19)$$

where the dimensionless function  $f(y) = ye^{-\gamma y}$ , the dimensionless variable  $y = v^2/v_0^2$ , and the dimensionless constant  $\gamma = \frac{\mu_{\alpha\beta} v_0^2}{2T}$ . The value  $v_0$  denotes the atomic velocity unit, as above, and  $\mu_{\alpha\beta} = m_\alpha m_\beta / (m_\alpha + m_\beta)$  is the reduced mass. The maximum of  $f(y)$  is attained at  $y = 1/\gamma$ . Assuming the cross-section  $\sigma(y)$  is a smoother function than  $f(y)$ , the integral in (19) can first be evaluated over a finite interval around the maximum of  $f(y)$ . Then, at every subsequent step, one should broaden the initially chosen arbitrary integration limits until the integral value becomes close enough to that obtained at the previous step. Thus, the required relative precision may be achieved.

Maxwellian fusion rate coefficients (19) are well known. Practical approximations for a number of reactions are given in [3] as functions of temperature. These approximations have been used for benchmarking to test the validity of general (*i.e.* not only for Maxwellian projectiles) subroutine (18). If a Maxwellian distribution is substituted in all-purpose formula (18) as a particular case of an isotropic function  $F(v_\alpha)$ , the result should agree with known Maxwellian rate coefficients taken from [3]. Such testing was done successfully and the correctness of the subroutine performing integration (18) has been verified.

#### 4. Fast Neutral Beam Injection-Induced Suprathermal Ion Distribution

To describe the neutral beam injection heating-induced fast ion distribution, one can use the classical non-stationary slowing-down distribution function  $F^{(sl)}(v_\alpha)$  for a delta-like fast ion source

$$S(v_\alpha - v_{inj}) = \frac{S_0}{4\pi v_\alpha^2} \frac{e^{-\frac{(v_\alpha - v_{inj})^2}{\epsilon}}}{\epsilon \sqrt{\pi}}. \quad (20)$$

expressed as

$$F^{(sl)}(v_\alpha) = \frac{K}{v_\alpha^3 + v_c^3} \left( erf \left( \frac{v^*(v_\alpha, t) - v_{inj}}{\epsilon} \right) - erf \left( \frac{v_\alpha - v_{inj}}{\epsilon} \right) \right). \quad (21)$$

where  $K$  is a normalization constant. The slowing-down time

$$\tau_s = \frac{3m_\alpha T_e^{3/2}}{4\sqrt{2\pi} n_e Z_\alpha^2 e^4 \Lambda m_e^{1/2}}. \quad (22)$$

and the cube of the critical velocity

$$v_c^3 = \frac{3\sqrt{2\pi} T_e^{3/2}}{2m_\alpha m_e^{1/2}}. \quad (23)$$

$\Lambda$  is the Coulomb logarithm, and, as shown in [6],

$$v^*(v_\alpha, t) = \left( (v_\alpha^3 + v_c^3) e^{3t/\tau_s} - v_c^3 \right)^{1/3}. \quad (24)$$

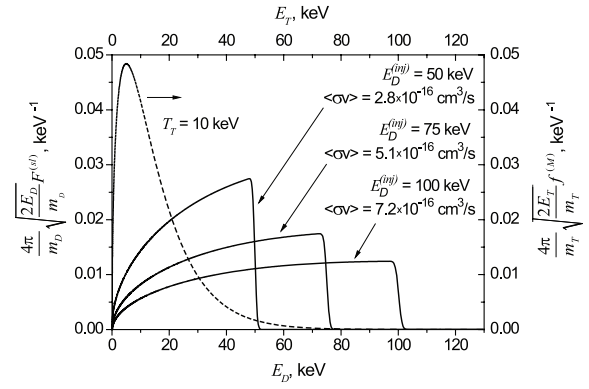


Fig. 4 Deuteron (solid curves) and triton (dashed curve) kinetic energy probability density functions and corresponding T(D,n)He4 fusion reaction rate coefficients.

The normalization constant  $K$  is determined by numerical integration. The ion velocity  $v_\alpha = \sqrt{2E/m_\alpha}$ ,  $v_{inj}$  is the injection velocity corresponding to the injection energy  $E^{(inj)}$ , the values  $S_0$  and  $\epsilon$  in (19) determine the source rate and peak width, respectively, and  $t$  is the time since the fast particle source action began.

Fig. 4 shows three examples of rate coefficients calculated using (18) for the interaction with isothermal Maxwellian tritium plasma;  $T_T = T_e = 10$  keV,  $n_e = 2.0 \times 10^{14} \text{ cm}^{-3}$ , and suprathermal deuterons are distributed according to (21) with injection energies  $E_D^{(inj)} = 50$  keV,  $E_D^{(inj)} = 75$  keV, and  $E_D^{(inj)} = 100$  keV. Unity-normalized triton (dashed curve) and deuteron (solid curves) energy probability density functions as well as the corresponding rate coefficient values for these three cases are shown.

#### 5. Treatment of Experimentally Obtained Suprathermal Ion Distributions

Radial and angle dependence of the ion distribution function is studied experimentally by means of passive line-integral and active localized charge exchange neutral particle diagnostics [7, 8]. An extensive diagnostic database of this kind should enable one to predict local ion distribution function evolution for a given plasma discharge regime in a certain device for a specific heating method and time diagram.

Using diagnostic data in the form of an array of energies ( $E_1, \dots, E_N$ ) of escaped neutral particles measured along a certain observation direction, where  $N$  is the total number of particles collected during a certain time interval, one can construct an empirical probability density function

$$f^{(e)}(E) = \frac{1}{Nh} \sum_{j=1}^N \mathcal{K} \left( \frac{E - E_j}{h} \right), \quad h > 0. \quad (25)$$

with Gaussian kernel function  $\mathcal{K}(z) = e^{-z^2/2} / \sqrt{2\pi}$ . Ion distribution function reconstruction and the algorithm for selecting an optimal kernel bandwidth  $h$  are discussed in

[9].

Thus, it is possible to perform a correct experimentally confirmed calculation of the time evolution of local fusion rate coefficient (4) and fusion reactor power (1). Specific MHD equilibrium data can then be used rather than analytic approximations.

Calculation of fusion rate coefficients using empirical probability density functions (25) is illustrated in Fig. 5. Rate coefficients have been calculated for the interaction between purely Maxwellian tritons at  $T_T = 10$  keV and 95 % Maxwellian deuterons with 5 % suprathermal tail distortion; *i.e.* the deuteron velocity probability density is

$$f_D^{(0)}(v) = 0.95f^{(M)}(v) + 0.05F^{(sl)}(v). \quad (26)$$

where superscript (0) denotes the absence of energetic particle losses. Furthermore, a model loss factor has been introduced in the form

$$f_D^{(\alpha)}(v) = f_D^{(0)}(v) \left(1 - \alpha e^{-\mu(v - \lambda v_{inj})^2}\right). \quad (27)$$

A sample of  $N = 5 \times 10^4$  uniformly distributed pseudorandom numbers has been generated using the Mersenne twister algorithm [10] and then recalculated to energy values ( $E_1, \dots, E_N$ ) by applying the inverse cumulative distribution function for the kinetic energy corresponding to velocity distribution (27) with  $\mu = 0.845 \times 10^{-16} \text{ s}^2/\text{cm}^2$ ,  $\lambda = 0.845$ , and three different values of the fast ion loss parameter:  $\alpha = 0$  (no losses),  $\alpha = 0.4$ , and  $\alpha = 0.6$ . The obtained numbers simulate random samples of deuterium particle energies measured during 1 s at N counts per second. Their 80-channel histograms are shown in Fig. 5. Such a reduction in the high-energy distribution tail may occur in practice due to fast particle confinement effects. Experimental observations of this kind were described in [11].

To evaluate the fusion reaction rate and also the effect of the difference in high-energy deuteron distribution tails on the fusion reaction rate, empirical probability densities

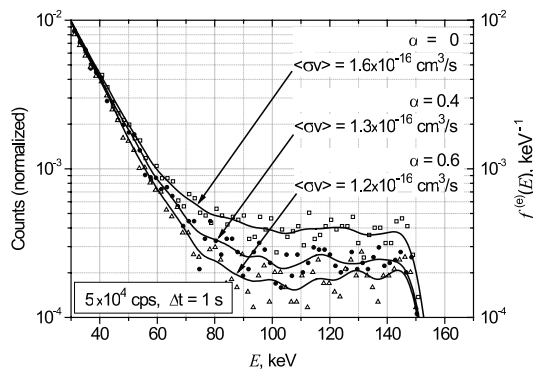


Fig. 5 Empirical probability density functions (curves) and histograms (points) for numerically simulated samples of pseudorandom deuteron energies corresponding to three loss parameter values:  $\alpha = 0$  (squares),  $\alpha = 0.4$  (solid circles) and  $\alpha = 0.6$  (triangles).

(25) have been calculated for the three random energy samples. They are shown by solid curves in Fig. 5. The corresponding  $T(D,n)\text{He}^4$  fusion reaction rate coefficients  $\langle \sigma v \rangle$  were calculated for each of the three cases by substituting the obtained empirical probability densities (25) into subroutine (18).

## 6. Power Calculation Examples

Assuming the radial density profiles to be

$$n_{e,D,T}(\rho) = (n_{e,D,T}(0) - n_{e,D,T}(1))(1 - \rho^a)^b + n_{e,D,T}(1). \quad (28)$$

and radial temperature profiles to be

$$T_{e,D,T}(\rho) = (T_{e,D,T}(0) - T_{e,D,T}(1))(1 - \rho^q)^r + T_{e,D,T}(1). \quad (29)$$

let us introduce an additive non-Maxwellian distortion in the form of (21) to the deuterium distribution so that

$$f_D(v_D) = A \left(\frac{m_D}{2\pi T}\right)^{3/2} e^{-\frac{m_D v_D^2}{2T}} + (1 - A)F(v_D). \quad (30)$$

where  $A \leq 1$ .  $A = 1$  corresponds to the pure undistorted Maxwellian case. The rate coefficient for the interaction of deuterium particles distributed according to (30),

$$\tilde{\mathcal{R}}_{DD} = A^2 \tilde{\mathcal{R}}_{DD}^{(MM)} (\mu_{DD}/T) + 2A(1 - A) \tilde{\mathcal{R}}_{DD}^{(FM)} + (1 - A)^2 \tilde{\mathcal{R}}_{DD}^{(FF)}. \quad (31)$$

is then calculated using (18) and (19). The last term in (31) accounts for the tail-tail particle interaction rate. It is considered negligible because the non-Maxwellian distortion is assumed to be small; *i.e.*,  $(1 - A)^2 \ll 1$ .

When a deuterium component distributed according to (30) interacts with Maxwellian tritons,

$$f_T(v_T) = \left(\frac{m_T}{2\pi T}\right)^{3/2} e^{-\frac{m_T v_T^2}{2T}}. \quad (32)$$

the rate coefficient is

$$\tilde{\mathcal{R}}_{DT} = A \tilde{\mathcal{R}}_{DT}^{(MM)} (\mu_{DT}/T) + (1 - A) \tilde{\mathcal{R}}_{DT}^{(FM)}. \quad (33)$$

The fusion rate radial profile and integral power calculations given below are for the  $T(D,n)\text{He}^4$  reaction. Fig. 6 shows the electron and ion temperature profile  $T_e = T_D = T_T$  with  $q = 1.5$ ,  $r = 2$ ,  $T_{e,D,T}(0) = 10$  keV, and  $T_{e,D,T}(1) = 50$  eV, and the electron density profile with  $a = 4$ ,  $b = 2$ ,  $n_e(0) = 1.0 \times 10^{14} \text{ cm}^{-3}$ , and  $n_e(1) = 0.7 \times 10^{14} \text{ cm}^{-3}$ . The nuclei densities are assumed to be  $n_D = n_T = n_e/2$ .

Calculations have been performed for three variants of the deuteron velocity distribution function shown in Fig. 7, namely, for an undistorted Maxwellian distribution and for a 2.5 % or 5 % population of suprathermal particles described by the classical slowing-down model of beam particles with injection energy  $E_{inj} = 150$  keV. The non-locality, *i.e.*, the radial dependence of the ion distribution

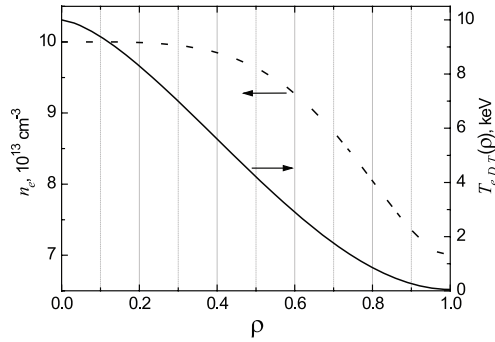


Fig. 6 Radial profiles of electron, deuteron, and triton temperatures and electron density.

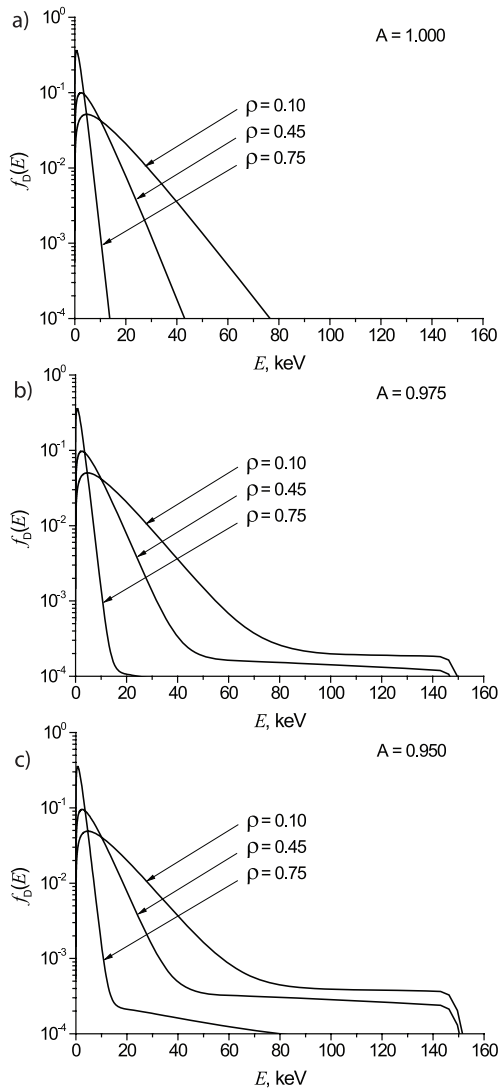


Fig. 7 Deuteron energy distribution function a) in undistorted Maxwellian case for  $A = 1$ , and in presence of suprathermal tail with b)  $A = 0.975$  and c)  $A = 0.950$ .

function, in this model is due to the radial profiles of  $n_e$  and  $T_e$ , which determine the slowing-down time and the critical velocity values.

For each of the three variants of the distribution, the

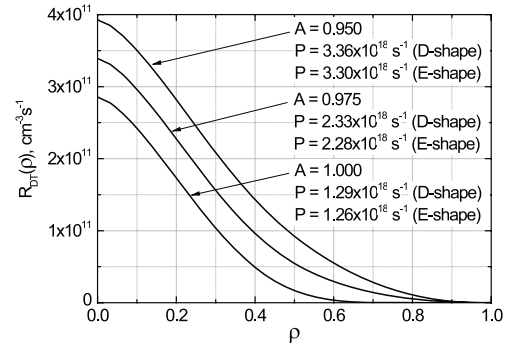


Fig. 8 Radial profiles of  $T(D,n)He4$  reaction rate for thermal tritons and three variants of deuteron energy distribution, and corresponding plasma volume integral power values for two types of magnetic surface geometry.

Table I Benchmarking against experiments.

Parameter	JET	TFTR
$R_{\text{major}}$ , m	2.96	2.60
$r_{\text{minor}}$ vert., m	2.10	0.90
$r_{\text{minor}}$ horiz., m	1.25	0.90
$n_e$ central, $m^{-3}$	$0.4 \times 10^{20}$	$0.8 \times 10^{20}$
$T_i$ central, keV	20	30
NBI tail	20 MW, 140 keV	30 MW, 120 keV
Reference	$P_{DD} = 4.0 \times 10^{16}$ neutron/s [12]	$P_{DT} = 9$ MW [13]
<b>Simulation</b>	$P_{DD} = 6.1 \times 10^{16}$ neutron/s	$P_{DT} = 12$ MW

radial profile of the  $T(D,n)He^4$  reaction rate has been calculated, as well as the plasma volume integral power for two types of magnetic surfaces with D-shaped and elliptical poloidal cross-sections as shown in Fig. 1. Slight differences in the magnetic surface shape, as expected, have no significant direct “geometrical” influence on the power. Calculation results are shown in Fig. 8. In this example, the presence of a 5% suprathermal deuteron population contributes significantly to the reaction rate and leads to an increase of approximately 2.6 times in the fusion power compared to the pure Maxwellian case. In similar conditions with a twice-lower central temperature  $T_{e,D,T}(0) = 5$  keV, the presence of 5% suprathermal deuterons would lead to an increase of more than 20 times in the fusion power and neutron yield. At a higher central temperature,  $T_{e,D,T}(0) = 20$  keV, this factor is about 1.3, since the Maxwellian rate prevails in this case.

For benchmarking purposes, our simulation results are compared with experiments on the JET (Joint European Torus) and TFTR (Tokamak Fusion Test Reactor) tokamaks [12, 13] and with design estimates for JT-60SA [14] and ITER [15] in Tables I and II, respectively. Benchmark-

Table II Comparison with design estimates.

Parameter	JT60-SA	ITER
$R_{\text{major}}$ , m	3.01	6.20
$r_{\text{minor}}$ vert., m	2.00	3.40
$r_{\text{minor}}$ horiz., m	1.14	2.00
$n_e$ central, $\text{m}^{-3}$	$1.0 \times 10^{20}$	$1.0 \times 10^{20}$
$T_i$ central, keV	10	20
NBI tail	34 MW, 150 keV	None (Maxwell)
Reference	$P_{\text{DD}} = 2.0 \times 10^{17}$ neutron/s [14]	$P_{\text{DT}} = 500$ MW [15]
<b>Simulation</b>	$P_{\text{DD}} = 1.3 \times 10^{17}$ neutron/s	$P_{\text{DT}} = 400$ MW

ing against experiments shows that our simulation, with about 50% accuracy, is more optimistic than the experimental results. However, our simulation results are below the design expectations, as seen in Table II.

## 7. Summary

A general practical algorithm has been realized to calculate the nuclear fusion rate and power in a toroidal magnetic plasma confinement device. Volume integration is performed using analytical approximations of magnetic surfaces. A detailed description of a velocity space integration technique for beam-Maxwellian, bi-Maxwellian, and isotropic function-Maxwellian cases has been given. Fusion rate and power calculations can be done using either theoretical or experimentally obtained nuclei energy distribution functions.

A significant contribution to the nuclear fusion reaction rates comes from suprathermal ions from high-energy distribution tails. Therefore, the production and good confinement of fast ions play an essential role. Reliable experimental data and theoretical understanding of the formation of fast ion distribution tails are required.

The ion distribution function reflects kinetic effects, single-particle confinement properties depending on the particular magnetic configuration, finite  $\beta$  effects such as MHD-induced fast ion losses, radial electric field effects, and other influences. As a method of investigating the ion component distribution function and its evolution upon application of heating, measurements of kinetic energy distributions of neutral atoms escaping from the plasma may be used; often referred to as neutral particle analy-

sis (NPA) diagnostics. Multidirectional passive measurements provide information on the angular anisotropy, fast ion confinement, and distribution tail shapes. Line-integral energy-resolved neutral fluxes are obtained at different observation angles. Special mathematical techniques are required for correct data analysis [7]. Another approach is to create a localized dense target for charge exchange in the plasma. A diagnostic pellet ablation cloud can be used for this purpose (pellet charge exchange, or PCX). Time-resolved measurements of the neutral flux from the cloud as it moves across the plasma column yield radially-resolved information on the fast particle energy distribution [8].

Smooth normalized probability density functions for the nuclei energies can then be calculated from NPA data using the method given in [9]. Thus, experimentally confirmed calculations of nuclear fusion rate and power are possible on the basis of diagnostic data.

This work was performed as a collaboration between Plasma Physics Department of St. Petersburg Polytechnic University and NIFS.

- [1] G.H. Miley, H. Towner and N. Ivich, Rept. COO-2218-17, University of Illinois (1974).
- [2] B.H. Duane, Rept. BNWL-1685, Brookhaven National Laboratory (1972).
- [3] H.-S. Bosch and G.M. Hale, Nucl. Fusion **32**, 611 (1992).
- [4] L.E. Zakharov, Preprint IAE-4114/6, Moscow (1985).
- [5] R.L. Miller, M.S. Chu, J.M. Greene, Y.R. Lin-Liu and R.E. Waltz, Phys. Plasmas **5**, 973 (1998).
- [6] J.G. Cordey and M.J. Houghton, Nucl. Fusion **13**, 215 (1973).
- [7] P.R. Goncharov, T. Ozaki *et al.*, Rev. Sci. Instrum. **79**, 10F311 (2008).
- [8] P.R. Goncharov, T. Ozaki *et al.*, Rev. Sci. Instrum. **79**, 10F312 (2008).
- [9] P.R. Goncharov, T. Ozaki *et al.*, Plasma Fusion Res. **3**, S1083 (2008).
- [10] M. Matsumoto and T. Nishimura, ACM Trans. Model. Comput. Simul. **8**, 3 (1998).
- [11] S. Murakami *et al.*, A Demonstration of Magnetic Field Optimization in LHD, IAEA-CN-94/EX/C5-3, 19th IAEA Fusion Energy Conference, Lyon, France, October, 2002.
- [12] C. Gormezano, Plasma Phys. Control. Fusion **41**, B367 (1999).
- [13] R.J. Hawryluk *et al.*, Phys. Plasmas **5**, 1577 (1998).
- [14] M. Matsukawa *et al.*, Engineering Feature in the Design of JT-60SA, FT/P7-5, 21st IAEA Fusion Energy Conference, Chengdu, China, October 2006.
- [15] M. Shimada *et al.*, eds., Nucl. Fusion **47**, S1 (2007).